Selective Response of the South China Sea Circulation to Summer Monsoon

HAIYUAN YANG AND LIXIN WU

Physical Oceanography Laboratory/CIMST, Ocean University of China and Qingdao National Laboratory for Marine Science and Technology, Qingdao, China

SHANTONG SUN

Scripps Institution of Oceanography, University of California, San Diego, La Jolla, California

ZHAOHUI CHEN

Physical Oceanography Laboratory/CIMST, Ocean University of China and Qingdao National Laboratory for Marine Science and Technology, Qingdao, China

(Manuscript received 28 December 2016, in final form 5 April 2017)

ABSTRACT

The response of the South China Sea (SCS) circulation to intraseasonal variability of the summer monsoon is studied with both observations and a 1.5-layer reduced-gravity model. Intraseasonal variability of the SCS summer monsoon is characterized by evolution of the wind jet intensity in the midbasin with typical amplitude of 6 m s^{-1} and several peaks on its power spectrum between 10 and 60 days. However, this study finds that intraseasonal variability of the sea surface height (SSH) in the SCS presents significant variability to the southeast of Vietnam with amplitude of 6 cm and a period only between 40 and 60 days. This implicates the frequency selectivity of oceanic response to wind forcing. Numerical experiments suggest that the intrinsic variability of the SCS circulation accounts for this phenomenon. Based on the Rossby basin mode theory, this is explained by the interaction between the long, westward-propagating Rossby waves and the short, eastward-propagating Rossby waves.

1. Introduction

As the largest marginal sea in the western tropical Pacific, the South China Sea (SCS) has a deep, semi-enclosed basin with an area of 3.5×10^6 km^2 (Fig. 1). Driven by the seasonal-varying monsoonal wind, the upper-layer circulation in the SCS is characterized by significant seasonal variation (Fang et al. 1998; Hu et al. 2000; Liu et al. 2008; D. Wang et al. 2013). During boreal winter, a basin-scale cyclonic circulation forced by the strong northeasterly monsoon emerges in the SCS Basin (Liu et al. 2004). Different from winter, the upper-layer circulation in the SCS Basin interior in summer presents a dipolar structure with a weak cyclonic gyre in the northern part of the SCS and a strong anticyclonic gyre in the south basin due to the southwesterly summer monsoon (Xie et al. 2003; Wang et al. 2006). Previous studies showed that both the establishment and large-scale variability of this double-gyre system is primarily subjected to the local wind within the SCS (S. Xie et al. 2007; Wang et al. 2010; Li et al. 2014) after a fast adjustment process associated with the first baroclinic mode Rossby waves (Liu et al. 2001; Wang et al. 2003).

Besides the seasonal variation, the southwesterly monsoonal wind in summer also exhibit prominent intraseasonal variability. From late May to early October, the summer monsoon is suggested to be controlled by two intraseasonal oscillation modes (Mao and Chan 2005; Wang et al. 2009): one with a broad period of 30–60 days (M30) and another one with a period of 10–20 days (M20). M30 is found to originate from the equatorial Indian Ocean and propagates northeastward. It plays an important role in the onset of monsoon and fluctuations of the low-level jets over Indian/Southeast Asia area (Murakami and Nakazawa 1984, 1985; Annamalai and Slingo 2001; S. Xie et al. 2007). Different from M30, M20 is generated in the Philippine Sea and migrates westward as atmospheric Rossby waves (Wang and Xie 1997;

Corresponding author: Haiyuan Yang, yanghaiyuan@ouc.edu.cn

DOI: 10.1175/JPO-D-16-0288.1

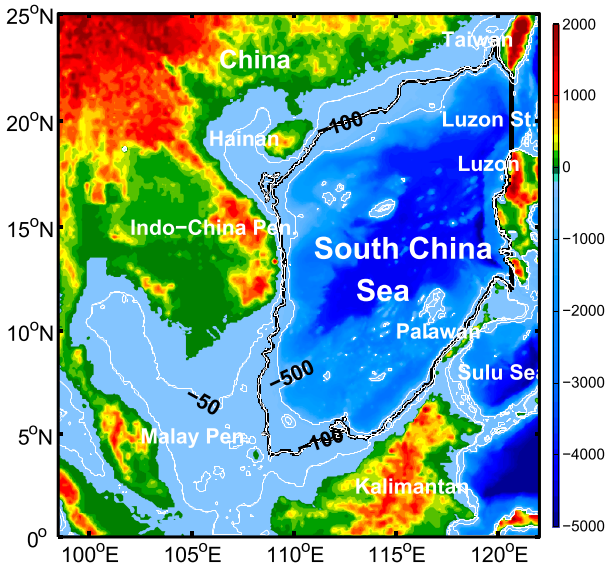

FIG. 1. Bottom topography of the SCS, with 50-, 100-, and 500-m isobaths shown. Black lines indicate the domain of 1.5-layer reduced-gravity model use in this study (100 m isobath).

Chatterjee and Goswami 2004). In general, the intraseasonal variability of the SCS monsoon is thought to be dominated by M30 and modified by M20, with M20 potentially being dominant when M30 becomes weak (Chen and Chen 1993, 1995; Chan et al. 2002; Mao and Chan 2005).

Influenced by the atmospheric forcing, the upper-layer circulation in the SCS Basin interior displays significant intraseasonal variability as well. Using both satellite altimeter observations and ocean models, S. Xie et al. (2007) found that the development of the double-gyre circulation in the deep basin of the SCS is not a smooth seasonal cycle but is characterized by several intraseasonal events at about 45-day intervals, which are associated with M30. Further analysis suggested that these events are controlled by Rossby wave adjustments that are excited by changes in wind forcing (S. Xie et al. 2007; Q. Xie et al. 2007; Zhuang et al. 2010). Moreover, Isoguchi and Kawamura (2006) and G. Wang et al. (2013) further studied the response of the SCS to wind perturbations caused by the Madden–Julian oscillation and found that it had an imprint on the summer SCS circulation with a period around 50 days. Associated with circulations, intraseasonal variability of heat flux and sea surface temperature in the SCS caused by monsoon are also estimated (Zeng and Wang 2009; Q. Xie et al. 2007; Roxy et al. 2013). However, all these studies highlighted the oceanic 45-day signal, which can be recognized as the signatures of M30, while it remains unclear why there is no intraseasonal variability corresponding to M20 in the SCS.

In this paper, the response of the upper-layer circulation in the SCS Basin interior to intraseasonal variability of summer monsoon is studied with both observations and a numerical model. Here, we will focus on the variability of the upper-ocean circulation in the SCS Basin interior that is purely induced by local wind forcing within the SCS, while the effects from the surrounding seas/oceans and complex topography will not be considered. This paper is organized as follows: Section 2 gives a brief description of the observed data and the numerical model. In section 3, a detailed analysis of the SCS intraseasonal variability is presented, followed by some dynamical explanations that employ the Rossby basin mode theory in section 4. The paper ends with a summary and further discussion in section 5.

2. Data and model

a. Sea surface height

The merged absolute dynamic topography (ADT) product, which is derived from measurements of two satellites [TOPEX/Poseidon (T/P) or *Jason-1* and ERS or *Envisat*], is used in this study. The data are distributed by Archiving, Validation, and Interpretation of Satellite Oceanographic Data (AVISO; http://www.aviso.oceanobs.com/). The merged ADT is better than a dataset using a single altimeter to resolve spatial and temporal variabilities of the ocean circulation, especially on mesoscale (Ducet et al. 2000). To reduce high-frequency aliasing, the dataset is updated with corrections using a new tidal model [Goddard/Grenoble Ocean Tide (GOT2000)] and a barotropic model [Modèle aux Ondes de Gravité 2-Dimensions Global (MOG2D-G)] in 2005 (Volkov et al. 2007; Dibarboure et al. 2008). The horizontal resolution of the data is ¼° at daily intervals. Here, we focus on the domain covering the SCS (0°–25°N, 100°–125°E) during the boreal summer (June to early October) from 1993 to 2015.

b. Atmospheric fields

To estimate the intraseasonal variability of summer monsoon, surface wind, and wind stress data derived from the European Centre for Medium-Range Weather Forecasts (ECMWF) interim reanalysis (ERA-Interim) product is used in this study (http://apps.ecmwf.int/datasets/data/interim-full-daily). Available from 1979 to the present, the product has a daily temporal resolution and ¾° horizontal resolution (Dee et al. 2011). Then the data are further transformed to the ¼° × ¼° version on the ECMWF's data server by performing linear

TABLE 1. Settings of numerical experiments.

Number	Wind forcing	Spinup	g' ($m\,s^{-2}$)	Straits
1	Daily ECMWF wind stress in the SCS (1993–2015)	Monthly mean ECMWF wind stress of December 1992 for 2 yr	0.03	All closed
2–16	Eq. (2)	23-yr mean (1993–2015) summer ECMWF wind stress for 2 yr	0.03	All closed
17–31	Replacing τ_{EOF1} with τ_{EOF2} in Eq. (2)	23-yr mean (1993–2015) summer ECMWF wind stress for 2 yr	0.03	All closed
32	Eq. (3)	23-yr mean (1993–2015) summer ECMWF wind stress for 2 yr	0.03	All closed
33	23-yr mean (1993–2015) summer ECMWF wind stress	23-yr mean (1993–2015) summer ECMWF wind stress for 2 yr	0.03	All closed
34–48	Eq. (2)	23-yr mean (1993–2015) summer ECMWF wind stress for 2 yr	0.036	All closed
49–63	Eq. (2)	23-yr mean (1993–2015) summer ECMWF wind stress for 2 yr	0.027	All closed
64	Daily ECMWF wind stress in the North Pacific Ocean only (1993–2015)	Monthly mean ECMWF wind stress of December 1992 for 20 yr	0.03	Opened Luzon Strait
65	Daily ECMWF wind stress in the North Pacific Ocean only (1993–2015)	Monthly mean ECMWF wind stress of December 1992 for 20 yr	0.03	Opened Luzon Strait and Mindoro Strait

interpretation for each latitude and longitude line (https://software.ecmwf.int/wiki/display/EMOS/Grid+point+to+Grid+point+Interpolation). Similar to the ADT data, the concurrent atmospheric fields between June and October during 1993–2015 within the region (0°–25°N, 100°–125°E) are used.

c. The 1.5-layer reduced-gravity model

Using a 1.5-layer, nonlinear, reduced-gravity model, multiple numerical experiments are performed to understand the relevant dynamics. The governing equations for this model are as follows:

$$\begin{cases} \dfrac{\partial u}{\partial t} + u\dfrac{\partial u}{\partial x} + v\dfrac{\partial u}{\partial y} - fv + g'\dfrac{\partial h}{\partial x} = A_H\nabla^2 u + \dfrac{\tau_x}{\rho(H+h)}, & \text{(1a)} \\ \dfrac{\partial v}{\partial t} + u\dfrac{\partial v}{\partial x} + v\dfrac{\partial v}{\partial y} + fu + g'\dfrac{\partial h}{\partial y} = A_H\nabla^2 v + \dfrac{\tau_y}{\rho(H+h)}, \quad \text{and} & \text{(1b)} \\ \dfrac{\partial h}{\partial t} + H\left(\dfrac{\partial u}{\partial x} + \dfrac{\partial v}{\partial y}\right) = 0. & \text{(1c)} \end{cases}$$

Here, u and v represent zonal and meridional velocity, respectively, H indicates the mean upper-layer thickness, h is the upper-layer thickness deviation with reference to H, f is the Coriolis parameter, g' denotes the reduced-gravity acceleration ($g' = g\Delta\rho/\rho$), A_H is the coefficient of horizontal eddy viscosity, ρ represents the reference water density, and τ_x and τ_y are the zonal and meridional surface wind stress. The horizontal resolution of this model is also 1/4°, and the model domain covers the deep basin (deeper than 100 m) of the SCS, which extends from 4° to 24°N in the meridional direction and from 108° to 120°E in the zonal direction (black line in Fig. 1).

No normal flow and nonslip boundary conditions are adopted. Some key parameters are as follows. The coefficient A_H is chosen as $500\,m^2\,s^{-1}$. The density difference between the lower layer and the upper layer $\Delta\rho = 3\,kg\,m^{-3}$ in the control run and the initial upper-layer thickness $H = 400$ m; thus, the phase speed of the first-order baroclinic Rossby wave [$c_R = \beta R_d^2 = \beta g'(H + h)/f^2$; here, R_d is the Rossby deformation radius and β is the meridional gradient of f] is approximately $0.33\,m\,s^{-1}$ at 11°N, which is consistent with previous estimations (Liu et al. 2001; S. Xie et al. 2007).

In this study, 65 model runs are conducted. In the control run (Exp1), the model is first spun up from rest using the monthly mean ECMWF wind stress of December 1992 for 2 yr. After spinup, the model is integrated for another 23 yr, forced by daily ECMWF wind stress spanning from

TABLE 2. Purposes of numerical experiments.

Number	Purposes
1	To validate the applicability of 1.5-layer reduced-gravity model in this study
2–16	To explore the behavior of the SCS to wind forcing with one particular frequency
17–31	To detect whether the patterns of wind forcing will influence the results in Exp2–16
32	To test the hypothesis that stronger longer-period variations of the ocean are due to a reddening of atmospheric white noise
33	To find the intrinsic period of the SCS
34–63	To test the robustness of our conclusion by varying g'
64	To estimate the role of the Pacific Ocean in influencing the variability in the SCS through the Luzon Strait
65	To estimate the role of the Pacific Ocean in influencing the variability in the SCS through the Luzon Strait and the Mindoro Strait

1993 to 2015, and the outputs are stored every day for analysis. In Exp2–63, the model is spun up from rest by the 23-yr mean summer monsoon for 2 yr. After that, the model is forced by steady or time-varying wind for additional 3 yr and daily output is used for analysis. In the above 63 runs, all straits connecting the SCS with surrounding seas/oceans are closed. As a discussion, part of the northwestern Pacific Ocean (4°–35°N, 120°E–180°) is added to the model domain with the opened Luzon Strait or Mindoro Strait in Exp64–65. Details of the setting of model experiments are summarized in Table 1, and the purposes for the runs are listed in Table 2. For more

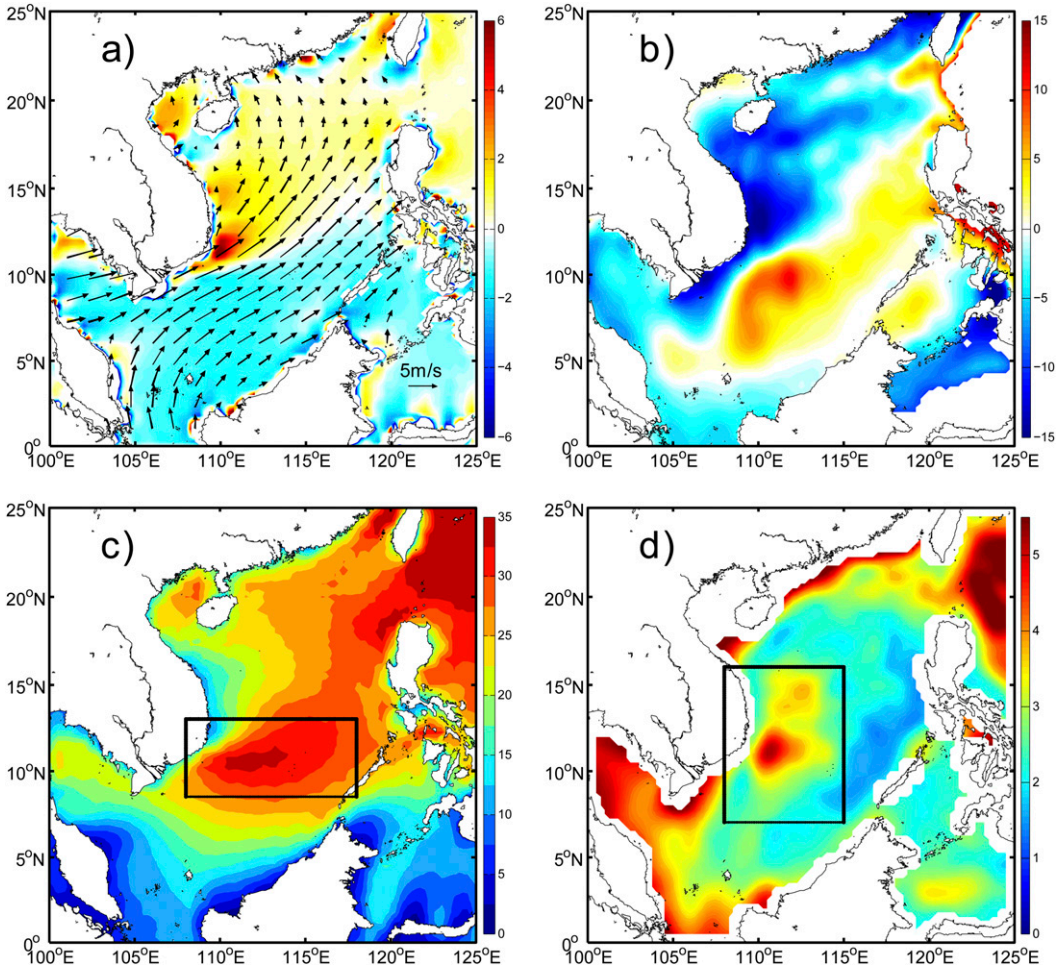

FIG. 2. Summer-mean (10 Jun–10 Oct) (a) surface wind (vectors, m s^{-1}) and WSC (shading, 10^{-7} N m^{-3}) from ECMWF and (b) SSH spatial anomaly (cm) fields from the T/P satellite during 1993–2015. Contemporaneous STD fields of (c) wind velocity squared (m^2 s^{-2}) and (d) SSH (cm).

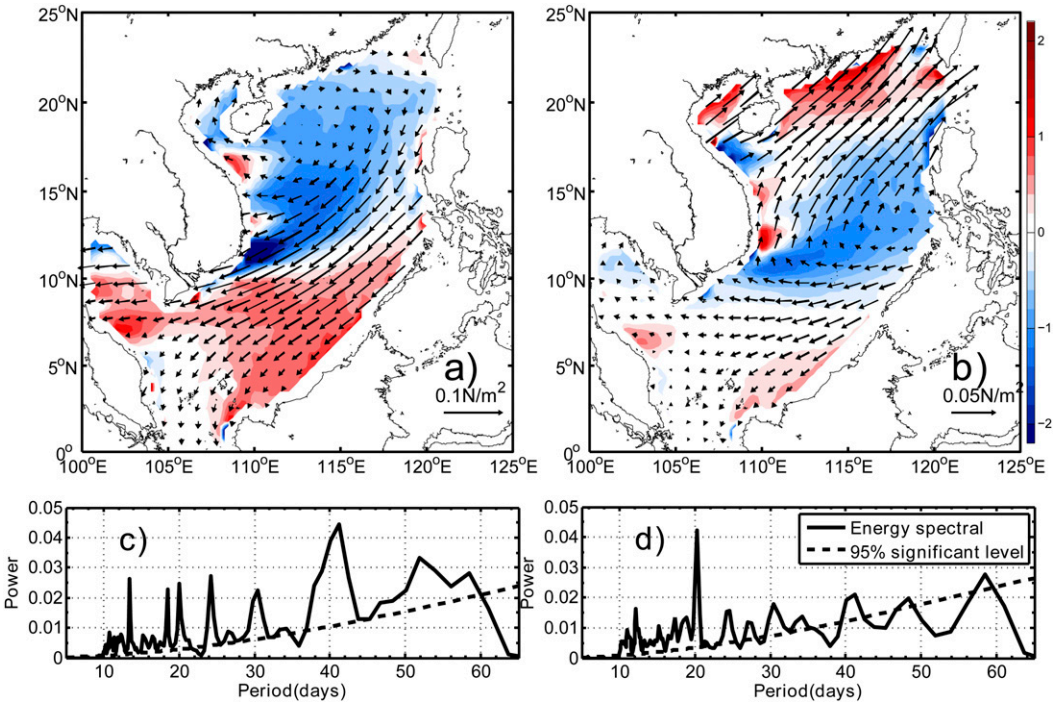

FIG. 3. (a) First and (b) second EOF modes of surface wind stress (vectors, $N\,m^{-2}$) of SCS summer monsoon within period band of 10–60 days and its associated WSC (shading, $10^{-7}\,N\,m^{-3}$). (c),(d) Energy spectra of the two modes.

information about the 1.5-layer reduced-gravity model, readers are referred to Chen and Wu (2011).

3. Intraseasonal variability of wind forcing and SSH fields in the SCS

a. Observations

Figure 2a shows the 23-yr mean summer (10 June to 10 October) wind velocity and wind stress curl (WSC). In summer, the southwesterly winds prevail in the SCS after the transition in late May to early June (Lau and Yang 1997). At about 12°N in the Indo-China Peninsula, the southwesterly winds are blocked by Annam Cordillera. Then the winds rush through at the southern tip of this mountain range, forming a strong wind jet offshore, to the east of Vietnam, with maximum speed over $10\,m\,s^{-1}$. In the SCS, this wind jet approximatively follows the straight line that connects 10°N, 110°E and 15°N, 118°E. Consequently, the axis of this wind jet separates the SCS into two parts, with the positive and negative WSC prevailing in the northern and southern part, respectively. Under the monsoon winds' forcing, the simultaneous mean SSH field derived from altimetry satellite is characterized by a double-gyre pattern (Fig. 2b), with a cyclonic gyre north of 11°N and an anticyclonic gyre in the south. Between these two gyres is an eastward current flowing northeastward, which plays an important role in regulating the oceanic dynamics and regional climate (Xie et al. 2003).

The standard deviations (STD) of wind velocity squared and SSH are displayed in Figs. 2c and 2d, respectively. The STDs are calculated from anomalies obtained by removing the climatological mean and the linear trend over 23 consecutive summers using a least squares method. Because this study is focused on the intraseasonal variability of 10–60-day periods, the variability that falls out of this band is filtered out. In the SCS Basin interior, the intraseasonal variability of wind velocity is strongest along the axis of the wind jet, with the maximum over $30\,m^2\,s^{-2}$ (Fig. 2c). According to S. Xie et al. (2007), this feature is mainly caused by variations of the wind jet intensity. Time-varying wind forcing leads to the generation of oceanic variability, which can be estimated by the STD of SSH fields (Fig. 2d). As we merely focus on the effect of local wind on the oceanic variability in this study, spatial 25-point average is performed for the SSH field before calculating STD to average out the signals of mesoscale eddies, which may influence the variability of SSH in that area (Zhuang et al. 2010; Chen et al. 2011). It is found that the intraseasonal variability of SSH is weakest in the southeast SCS and strongest in the western SCS close to Vietnam. The strong variability in the west SCS is thought to

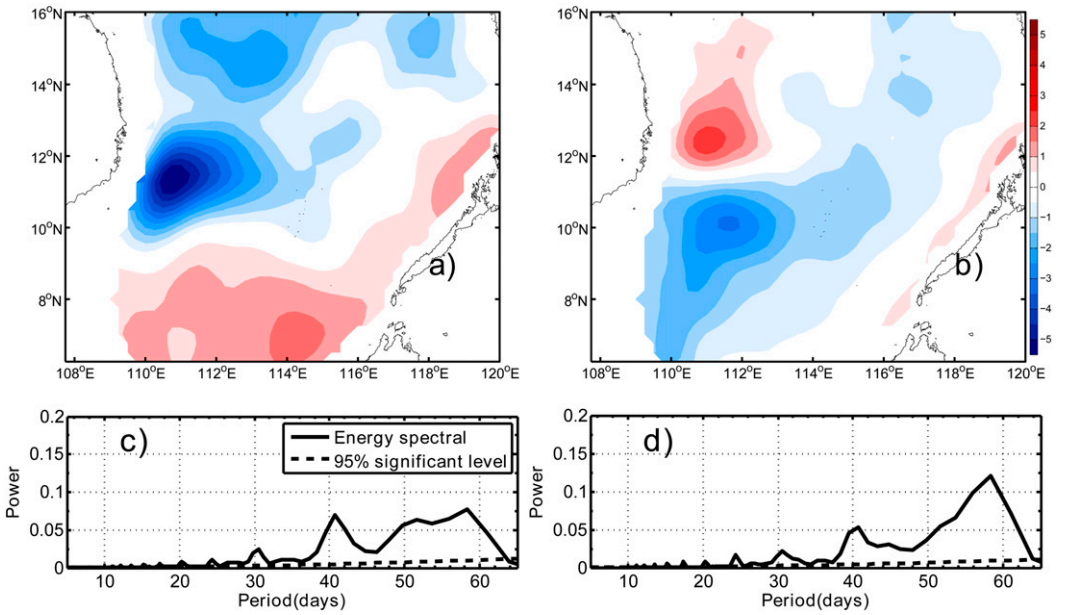

FIG. 4. (a) First and (b) second EOF modes of 25-point-averaged SSH field (cm) within period band 10–60 days in the SCS during summer. (c),(d) Energy spectra of the two modes.

be associated with the instability of the eastward current between the two gyres (Yang et al. 2013).

The EOF method is performed to extract the dominant patterns of atmospheric and oceanic variability. As in the calculation for STD, 10–60-day bandpass filtering is also performed before EOF decomposition. The leading EOF pair of summer monsoon contains about 65% (38% and 27%) of the total variance. The spatial

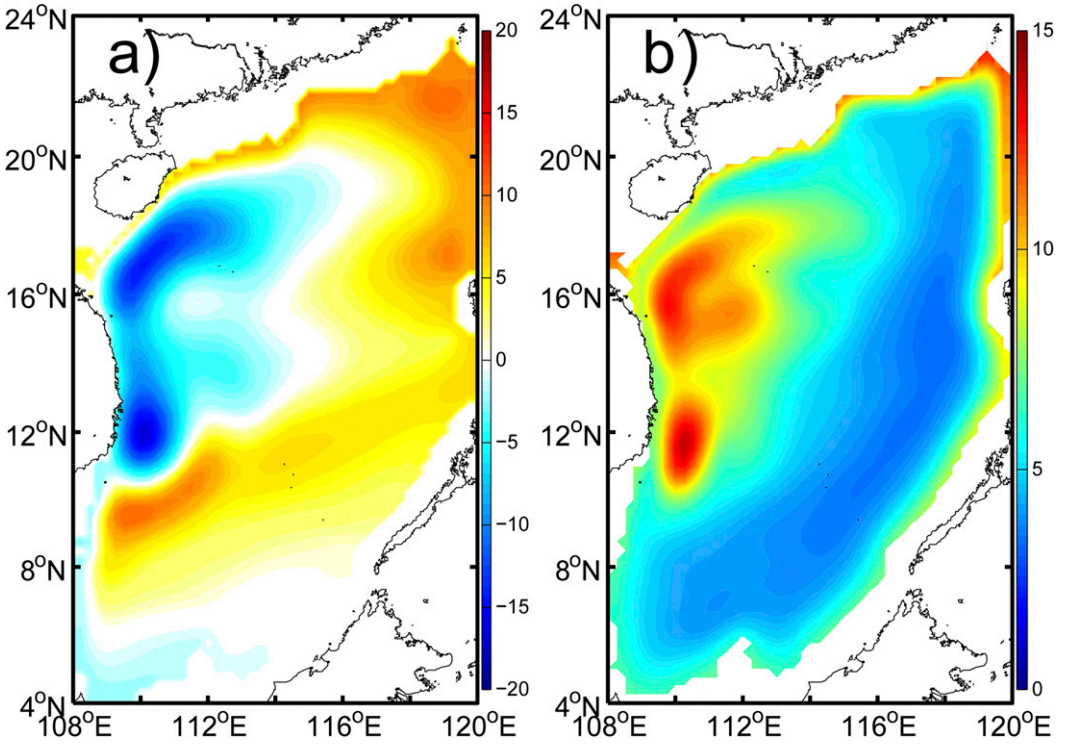

FIG. 5. Summer-mean (10 Jun–10 Oct) (a) upper-layer thickness deviation h (m) derived from Exp1 and (b) its contemporaneous STD fields.

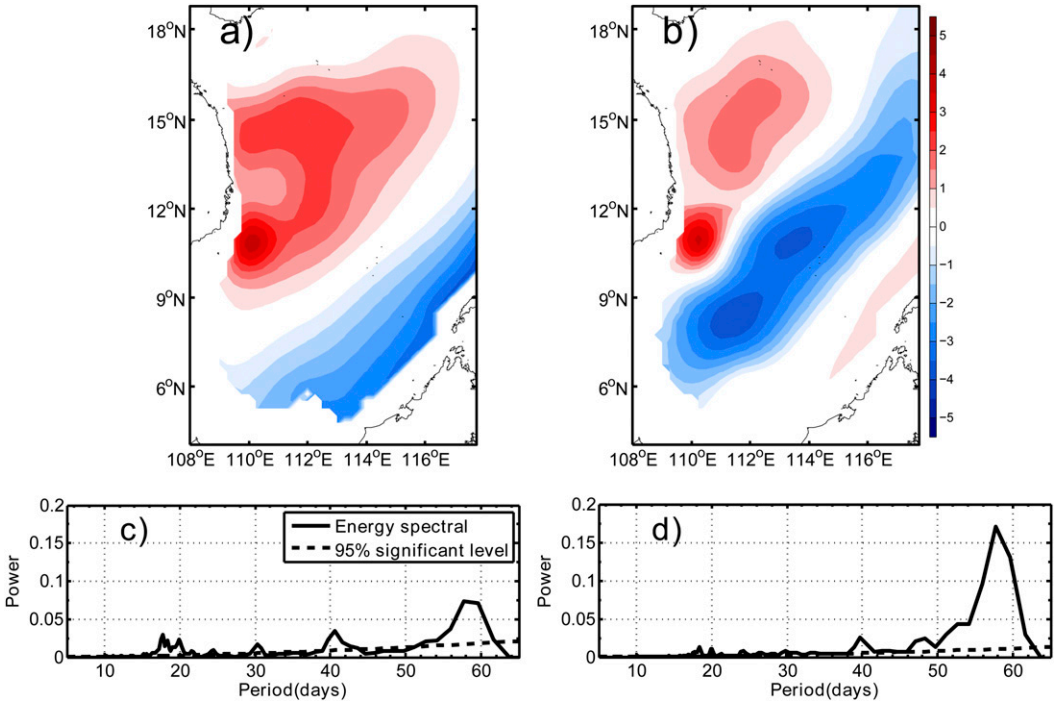

FIG. 6. (a) First and (b) second EOF modes of h field (m) within period band of 10–60 days in the SCS during summer derived from Exp1. (c),(d) Energy spectra of these two modes.

distribution of the first mode depicts southwesterly wind anomalies with a dipolar structure in the WSC, which captures well the variations of summer monsoon intensity (Fig. 3a). Differently, the second mode is characterized by a basin-scale anticyclonic pattern that is associated with the shift of wind jet (Fig. 3b). The power spectra of both modes are characterized by several peaks between 10 and 60 days, indicating the wide spectral characteristics of the SCS summer monsoon. The dominated period of the first mode is 40 days, while that of the second mode is 20 days (Figs. 3c,d). The results of EOF analysis resemble the conclusion of Mao and Chan (2005) that both M20 and M30 play important roles in regulating the SCS summer monsoon.

In a similar analysis that is performed to the 25-point-averaged summer SSH, two leading EOF modes (Figs. 4a,b) are recognized, which account for 22% and 12% of the total variance, respectively. Notice that only the regions south of 16°N and water deeper than 200 m are used here to avoid the influence from eddies at the Luzon Strait (Jia and Liu 2004) and the uncertainties induced by satellite observations in the nearshore area. The first mode of SSH presents a negative center around 11.5°N, 111°E, while the second mode is characterized by a dipolar pattern, which is asymmetric with respect to the latitude line of 11.5°N. Unlike the intraseasonal variability of the monsoon, both of these two modes are characterized by variabilities of periods between 40 and 55 days (Figs. 4c,d). The correlations of these two modes with the first EOF mode of summer monsoon are 0.5 and 0.4, respectively, which are significant at the 99% confidence level [the effective numbers of freedom of the bandpassed time series are larger than 40 (Bretherton et al. 1999), and the 99% confidence level is 0.39; hereinafter, all the correlations are significant at the 99% confidence level]. Although both M30 and M20 are important in the wind variability, only the footprint of M30 is found in the ocean. Next, we use a numerical model to investigate the oceanic response to variabilities of different frequencies.

b. *Model estimation*

Before exploring the mechanism of intraseasonal variability in the SCS, it is necessary to see whether the model can capture the frequency selectivity of the ocean as observed in SSH. This is easier to justify with some quantification of M30/M20 as discussed later. The summer-mean circulation in the SCS from Exp1 is characterized by a double-gyre pattern accompanied by an eastward current between them (Fig. 5a). The upper-layer thickness deviation h is 15 and −20 m for the anticyclonic and cyclonic gyre, respectively, which is in agreement with previous modeling studies (Wang et al. 2006). Similar to the satellite observations (Fig. 2d), the

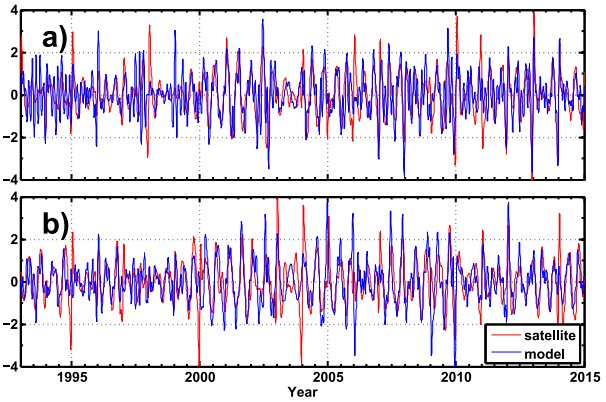

FIG. 7. (a) Normalized PC of first EOF mode derived from satellite (red) and 1.5-layer model (blue). (b) As in (a), but for the second EOF mode. Correlations between curves in (a) and (b) are 0.66 and 0.63, respectively.

intraseasonal variability of h is weakest in the eastern SCS and strongest to the southeast region of Vietnam at around 11°–12°N (Fig. 5b). Considering the relationship of $\mathrm{SSH}'/h' = g'/g$, the 15-m amplitude of h' corresponds to a 4.5-cm fluctuation of the SSH′, which is comparable to the results in Fig. 2. To validate the 1.5-layer reduced-gravity model in simulating the SCS intraseasonal variability, we also perform the EOF analysis on the model output (Fig. 6). The leading EOF pair, which explains 28% and 15% of total variance, shows similar patterns and explained variance compared with observations. Correlations between principal components (PCs) of these two modes and their counterparts derived from satellites exceed 0.6 (Fig. 7). Similar to altimetry observations, the signal of M30 is much stronger than M20 by the ocean. In general, the 1.5-layer reduced-gravity model reasonably captures both the mean state and intraseasonal variability of the SCS summertime circulation. In the following section, we will explore the dynamical mechanisms.

4. Mechanism

In this section, we explore the behavior of the SCS circulation in response to variabilities of wind forcing that have different frequencies. First, we perform 15 numerical experiments to explore the behavior of the SCS forcing by wind oscillations with the same pattern but different frequencies (Exp2–16). As the first EOF mode dominates the intraseasonal variability of summer monsoon, its spatial distribution is used to represent the pattern of wind oscillations. To avoid the superposition of frequency, wind forcing is characterized with one particular frequency in each run. For Exp$k$, the wind forcing field is in forms of

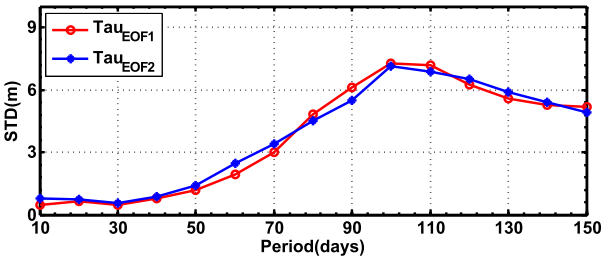

FIG. 8. Variations of mean STD of h in region 7°–16°N, 108°–115°E (black rectangle in Fig. 2d) with a period of wind forcing. Red and blue curves represent experiments forced with $\boldsymbol{\tau}_{\mathrm{EOF1}}$ and $\boldsymbol{\tau}_{\mathrm{EOF2}}$, respectively.

$$\boldsymbol{\tau} = \boldsymbol{\tau}_{\mathrm{mean}}(x,y) + \boldsymbol{\tau}_{\mathrm{EOF1}}(x,y)\cos\frac{2\pi}{(k-1)\times 10\ \mathrm{days}}t,$$
$$k = 2,3\ldots 16, \tag{2}$$

where $\boldsymbol{\tau}_{\mathrm{mean}}$ is 23-yr mean surface wind stress during summertime (10 June–10 October), and $\boldsymbol{\tau}_{\mathrm{EOF1}}$ is the spatial distribution of the first EOF mode of the summer monsoon derived from ECMWF (Fig. 3a). Here, the intensity of ocean circulation variabilities in response to atmospheric variability are represented by the mean STD of h in the region 7°–16°N, 108°–115°E (black rectangle in Fig. 2d), where the oceanic instability reaches its maximum. Figure 8 illustrates the variation of area-mean STD, in which the curve (red) depicts a unimodal structure that reaches its maximum at a period of 100 days. This indicates that the ocean prefers a time scale of 100 days. To further test the sensitivity of this period to wind oscillation patterns, we replace $\boldsymbol{\tau}_{\mathrm{EOF1}}$ with $\boldsymbol{\tau}_{\mathrm{EOF2}}$ (spatial distribution of the second EOF mode of summer monsoon; Fig. 3b) in Exp17–31, and similar results are also found (the blue curve in Fig. 7). This suggests that this period is not influenced by the pattern of wind oscillation. Moreover, it is found that for both the wind oscillations, STD values within the span 30–60 days are much larger than those in 10–25 days, resembling the feature derived from Exp1.

Previous studies implied the possibility that stronger response of the SCS to wind forcing at 30–60 days than at 10–25 days is caused by the reddening of atmospheric white noise (Frankignoul 1979; Frankignoul et al. 1997). To test this hypothesis, we perform Exp32 with wind forcing:

$$\boldsymbol{\tau} = \boldsymbol{\tau}_{\mathrm{mean}}(x,y) + \boldsymbol{\tau}_{\mathrm{EOF1}}(x,y)y(t), \tag{3}$$

where $y(t)$ represents a white noise time series. Figure 9 presents the dominant EOF mode derived from Exp32,

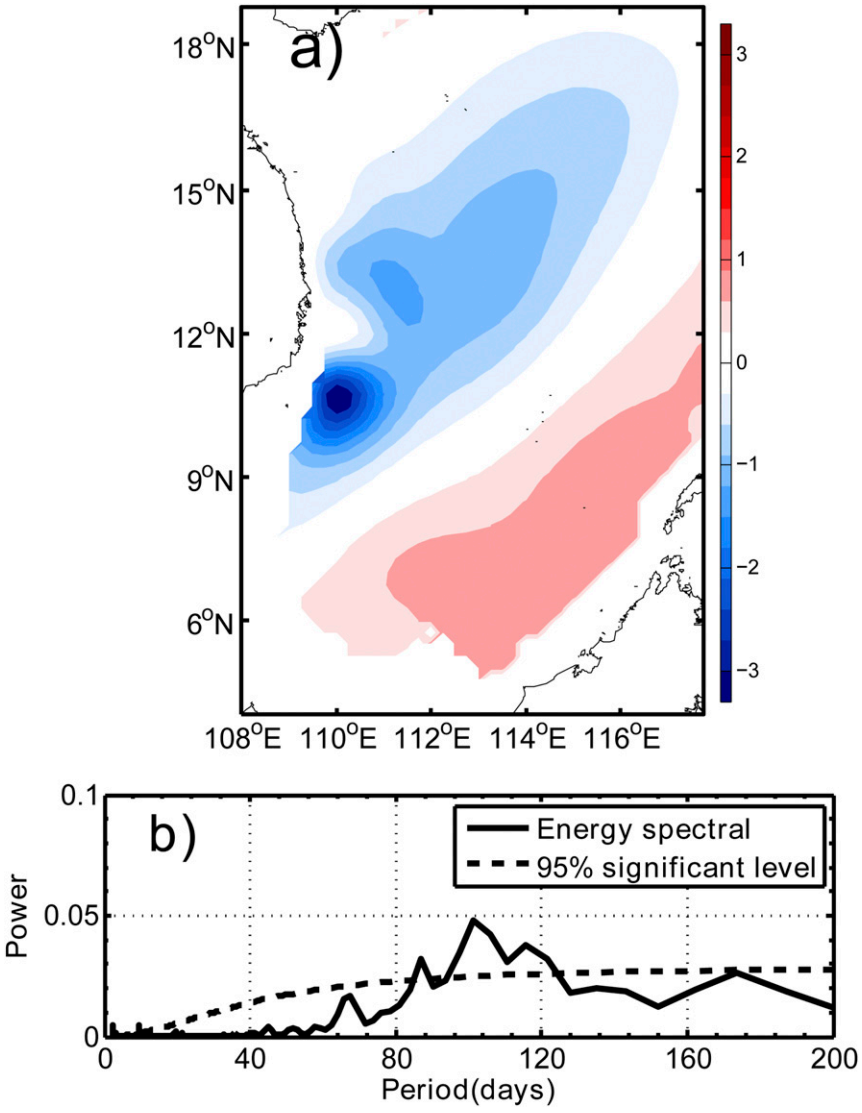

FIG. 9. (a) The first EOF mode of the h field (m) in the SCS derived from Exp32. (b) Energy spectra of this mode.

which explains 34% of the total variance. As opposed to the result based on linear theory of stochastic forced variability, which speculates a red-noise response, the spectral of this mode is characterized by a unimodal pattern with the peak around 100 days, proving that there indeed exists a preferred time scale in the SCS.

The preferred variability frequency period derived from the numerical experiments is close to the time scale of the SCS adjustment suggested by Bayler and Liu (2008), implying that this preferred period is the intrinsic period of the SCS Basin. We test this hypothesis by forcing the SCS with steady summer monsoon $\boldsymbol{\tau}_{\text{mean}}$ in Exp33 and perform EOF analysis to h, which yields two leading EOF modes that account for 53% and 40% of the total variance, respectively (Fig. 10). Both modes depict wavelike patterns in the zonal direction with a period of 104 days. Considering the pattern of the mean circulation, these modes embody the wave adjustment process and are manifested by variations of the eastward jet area. The magnitude of correlation between the time series of these two modes reaches the maximum 0.95 at ±25 days (about one-quarter of the dominant period), suggesting that the signal is nearly periodic. It is also found that the waves in Figs. 10a and 10b are slightly tilted toward the northeast–southwest, which may be caused by the latitudinal variation of their phase speeds.

The wavelike patterns are compared with the Rossby basin mode suggested by Cessi and Louazel (2001).

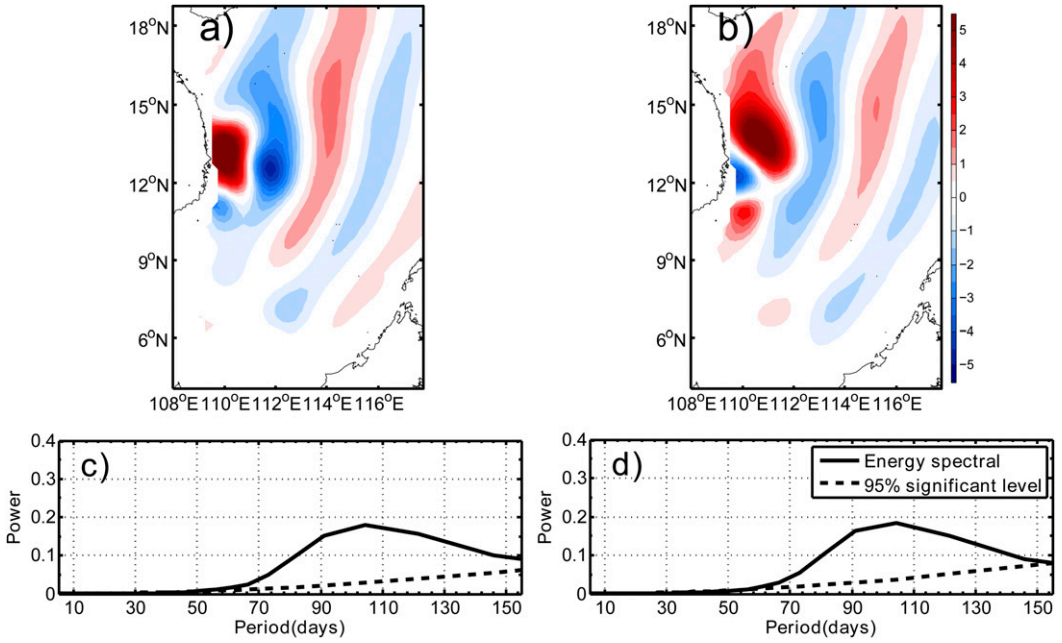

FIG. 10. (a) First and (b) second EOF modes of the h field (m) in the SCS derived from Exp27. Energy spectra of these two modes are shown in (c) and (d), respectively.

Considering the 1.5-layer baroclinic planetary wave model,

$$\frac{\partial h}{\partial t} + (U - c_R)\frac{\partial h}{\partial x} = -W_e, \quad \text{and} \tag{4a}$$

$$c_R = \beta \frac{g'(H+h)}{f^2}, \tag{4b}$$

where U and c_R are zonal-mean eastward velocity and phase speed of first-order baroclinic Rossby waves, respectively. Both U and c_R are obtained from the 1.5-layer reduced-gravity model. The variable W_e is the Ekman pumping velocity. Compared to the equation used in Cessi and Louazel (2001), the role of background current U in affecting oceanic variability is considered here. This is necessary in the SCS because the jet between two gyres is relatively strong. To simplify the calculation, the SCS Basin within the region of 4°–23°N, 110°–119°E is treated as a closed rectangle with a domain 950 km wide and 2000 km long. Following Cessi and Louazel (2001), W_e is set to be

$$W_e = W_0 \omega(t) F(y). \tag{5}$$

Here, $F(y)$ is the meridional distribution of Ekman pumping velocity, which is calculated from ECMWF data, and $\omega(t)$ is a random number generated at every time step from a standard Gaussian distribution. Under the constraint of mass conservation, the Fourier transform of Eq. (4a) gives

$$\hat{h}_0(\sigma) = \frac{\int_0^{L_y} -F\{L_x - i\sigma^{-1}(U-c_R)[e^{-i\sigma L_x/(U-c_R)} - 1]\}\, dy}{\hat{\omega}\int_0^{L_y} \{(U-c_R)[e^{-i\sigma L_x/(U-c_R)} - 1]\}\, dy}, \tag{6}$$

where $\hat{h}_0(\sigma)$ is defined as the Fourier transform of h_0, upper-layer thickness deviation along the eastern boundary, and the hat indicates the Fourier transform. The spectrum is obtained by calculating the square of the absolute value of Eq. (6) and ensemble averaging with $\overline{|\hat{\omega}^2|} = 1$ (Fig. 11). According to Fig. 11, the preferred time scale of response for the SCS summer

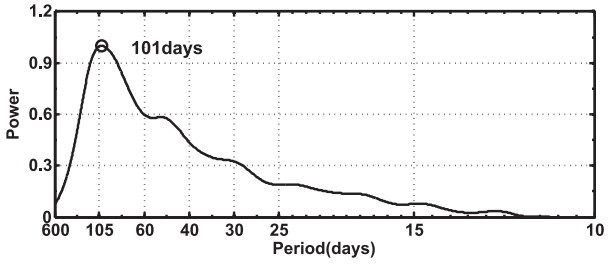

FIG. 11. Power spectrum of upper-layer thickness deviation along eastern boundary $h_0(t)$ calculated based on eigenmodes analysis. The spectrum peaks at 101 days.

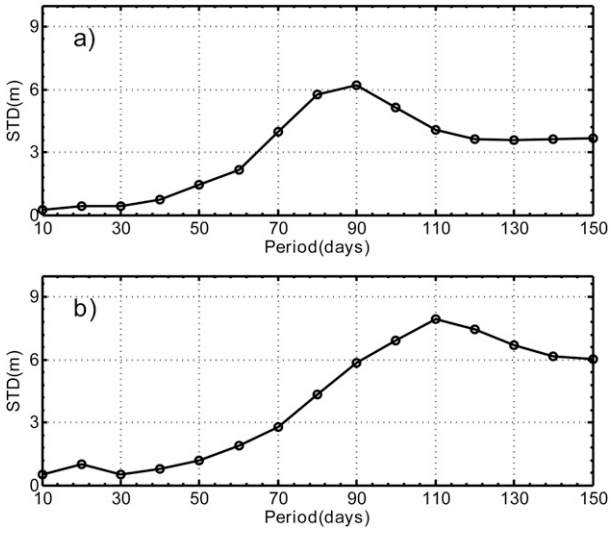

FIG. 12. The red curve as in Fig. 8, but for g' = (a) 0.036 and (b) 0.027 m s^{-2}.

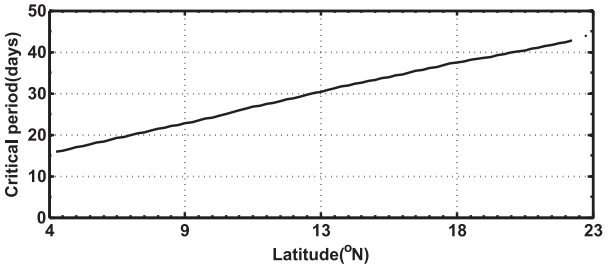

FIG. 13. Variations of critical period T_c (days) with the latitude in the summer SCS.

circulation is found to be 101 days, which is very close to the peak period shown in Fig. 10. The consistency between the theoretical analysis and model outputs suggests that the intraseasonal variability of the SCS summer circulation is dominated by the linear Rossby wave adjustment process.

According to Cessi and Louazel (2001), the time scale of the oceanic intrinsic variability is determined by the transit time of the slowest Rossby wave across the basin. We have estimated this transit time at different latitudes in the SCS, and it is shown that the transit time curve peaks at around 16°N with the maximum at 106 days (not shown), consistent with the results from the theoretical calculation. Moreover, we modify c_R in the model by varying g' in several sensitivity experiments. In Exp34–48 and Exp49–63, we set g' to be 0.036 and 0.027 m s^{-2}, respectively, but keep the wind forcing the same as Exp2–16. Under this setting, the longest transit time reduces/increases to 88/113 days. Figure 12 shows the variations of STD with different periods of wind forcing. Compared to Fig. 8, the peaks of the curves move to 90 and 110 days in Figs. 12a and 12b, respectively, which are in good agreement with the expected results derived from theoretical analysis. To further prove that this process does work in the SCS, we calculate the dissipation time scales of eastward Rossby waves, which are essential for the basin mode (Pedlosky 1987; see the appendix). It is found that it takes about 120 days for the horizontal viscosity to wipe out the eastward Rossby waves, which is larger than the time scale of basin mode (100 days). Thus, it is likely that this theory is applicable in the SCS.

According to the above analysis, we briefly explain the physical processes regarding the selectivity of ocean response to wind oscillations. At intraseasonal time scale, the atmospheric variability is dominated by two signals with approximately equal strength, that is, M30 and M20. However, because the period of M30 is closer to the intrinsic period of the SCS (about 100 days), at which the resonance between ocean adjustment and atmosphere oscillation is achieved, the magnitude of oceanic variability induced by M30 is much larger than that caused by M20.

5. Summary and discussion

Based on both observations and the reduced-gravity model, the response of the upper-layer SCS to intraseasonal variability of wind forcing during summertime is studied. The major results of this study are summarized as follows:

1) Intraseasonal variability of the SCS summer monsoon is dominated by two oscillations, that is, M30 and M20. The variability of SSH is only significant at the period of 40–60 days, implying the selectivity of the ocean response to wind forcing.
2) Numerical experiments indicate that the preferred period of ocean response is around 100 days, which is determined by the Rossby basin mode associated with the interaction between the long, westward-propagating Rossby waves and the short, eastward-propagating Rossby waves. As the period of M30 is closer to this intrinsic period, the oceanic signal induced by M30 is much stronger than by M20.

In addition, the selectivity of the ocean response can also be understood in terms of the critical period of the free first baroclinic mode Rossby waves (Lin et al. 2008). Based on this theory, the period of free Rossby waves has a minimum value $T_c = (4\pi f)/(\beta\sqrt{g'H})$. On one hand, for those atmosphere oscillations with a period smaller than the critical period T_c, the Rossby waves

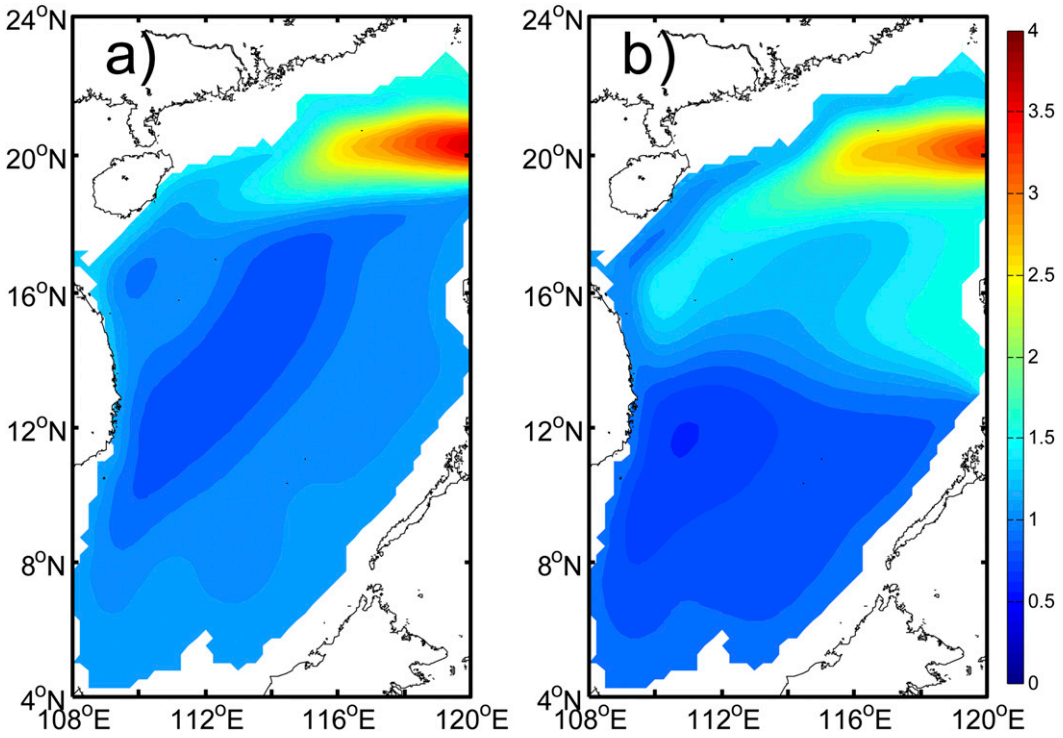

FIG. 14. As in Fig. 5b, but for (a) Exp64 and (b) Exp65.

do not exist. On the other hand, for those with a period larger than the T_c, both long and short oceanic Rossby waves transmit the signal from the atmosphere into the ocean interior. Figure 13 shows the critical period for each latitude in the SCS, and it is found that the critical period reaches 25 days at around 10°N, indicating that M20 cannot excite free Rossby waves north of 10°N. In comparison, M30 can regulate the circulation in the whole SCS, as the critical period T_c is always less than 45 days. This difference may serve as another factor that leads to the selectivity of the SCS response to wind forcing.

Previous studies have suggested that the Pacific Ocean may affect the intraseasonal variability of the SCS circulation through the Luzon Strait and the Mindoro Strait (Liu et al. 2011; Nan et al. 2015). To examine this effect, we compute two additional solutions with the northwestern Pacific basin involved in the model domain (Fig. 14). In the first run, the SCS and the North Pacific are only connected by the Luzon Strait (Exp64), while they are connected by both the Luzon Strait and the Mindoro Strait in the second run (Exp65). In Exp64, high STD values are found confined to the area north of 19°N where the Kuroshio intrusion occurs, while magnitudes of STD are very small in the SCS Basin interior. Compared to that, STD is significantly larger within the latitudinal band 13°–19°N when the Mindoro Strait is opened. Two factors may be responsible for this. On one hand, the northern branch of SCS through flow is established. Water from the Pacific Ocean flows into the SCS through the Luzon Strait and leaves the SCS at the Mindoro Strait, forming a cyclonic circulation in the northern SCS (not shown). Variability of this circulation, such as evolution of transport or pathway, will enlarge the STD. On the other hand, oceanic variability at the Mindoro Strait excites coastal Kelvin waves that propagate northward along the west coast of the Philippines and Rossby waves that propagate westward (Liu et al. 2011). Magnitude of STD is 1.5 m in the northern SCS, accounting for 10% of that caused by the monsoonal wind in the SCS. This suggests that the water exchange with the Pacific Ocean plays a secondary role in regulating the SCS intraseasonal variability. In addition to the Mindoro Strait, the Karimata Strait is also an important constituent part of the interaction between the SCS and surrounding waters. We speculate the STD will be larger when the Karimata Strait is opened. However, the depth of the Karimata Strait is less than 50 m; thus, the 1.5-layer reduced-gravity model is not applicative in this area. This will be further explored in detail with the ocean general circulation model.

Acknowledgments. This research is supported by National Natural Science Foundation of China Project (41490640, 41490643, 41622602, U1606402), Funds for

Creative Research Groups of China (41521091), National Key Scientific Instrument and Equipment Development Projects of China (41527901), WenHai Project of Shandong Province (2016WH03ZR), Special Fund for the Strategic Priority Research Program of the Chinese Academy of Sciences (XDA11010101), Global Change and Air-Sea Interaction Project (GASI-03-01-01-05), Fundamental Research Funds for the Central Universities (201713022), and National Science Foundation of the United States (OCE-1357078). The authors wish to thank Prof. Jiayang Yang, Prof. Bo Qiu, and Prof. Xiaopei Lin for helpful advice. Comments from two anonymous reviewers are greatly appreciated.

APPENDIX

Mechanism of the Rossby Basin Mode

Considering the quasigeostrophic equations,

$$\frac{\partial}{\partial t}\left(\nabla^2\psi - \frac{1}{R_d^2}\psi\right) + \beta\frac{\partial\psi}{\partial x} = 0. \tag{A1}$$

Here, ψ represents the streamfunction. Let $\psi(x, y, t) = \mathrm{Re}e^{-i\sigma t}\Phi(x, y)$ and we obtain

$$\nabla^2\Phi + \frac{i\beta}{\sigma}\frac{\partial\Phi}{\partial x} = 0. \tag{A2}$$

The notation Re means real part. Then, making variable substitution by $\Phi(x, y) = e^{-\beta x/2\sigma}\phi(x, y)$, we get the Poisson equation

$$\nabla^2\phi + \left(\frac{\beta^2}{4\sigma^2} - \frac{1}{R_d^2}\right)\phi = 0. \tag{A3}$$

Assuming that the SCS is a closed rectangle with a domain of $L_x = 950$ km and $L_y = 2000$ km, we get the eigenvalues of this system:

$$\begin{cases} \phi = \sin\dfrac{m\pi}{L_x}x\sin\dfrac{n\pi}{L_y}y, \quad m, n = 1, 2\ldots & \text{(A4a)} \\ \sigma = \dfrac{\beta}{2\pi}\left(\dfrac{m^2}{L_x^2} + \dfrac{n^2}{L_y^2} + \dfrac{1}{\pi^2 R_d^2}\right)^{-1/2}, & \text{(A4b)} \\ T = \dfrac{4\pi^2}{\beta}\left(\dfrac{m^2}{L_x^2} + \dfrac{n^2}{L_y^2} + \dfrac{1}{\pi^2 R_d^2}\right)^{1/2}, \text{ and} & \text{(A4c)} \\ \psi = \cos\left(\dfrac{\beta}{2\sigma}x + \sigma t\right)\sin\dfrac{m\pi}{L_x}x\sin\dfrac{n\pi}{L_y}y. & \text{(A4d)} \end{cases}$$

Here, we choose R_d to be 10^5 m based on the reality of the SCS. According to Eq. (A4c), T is close to 100 days when $m = 3$ and $n = 1$. The corresponding short-wave vector is $\mathbf{K} = \{-[\beta/(2\sigma)] - [(3\pi)/L_x]\}\mathbf{i} \pm (\pi/L_y)\mathbf{j}$.

Then, considering the quasigeostrophic equations with time tendency and dissipation term,

$$\frac{\partial}{\partial t}\left(\nabla^2\psi - \frac{1}{R_d^2}\psi\right) = A_H\nabla^4\psi. \tag{A5}$$

Taking in ψ derived from Eq. (A4), the scale of the terms in the bracket on the left-hand side of Eq. (A5) is

$$O\left\{\max\left[\left(\frac{\beta}{2\sigma}\right)^2, \left(\frac{3\pi}{L_x}\right)^2, \frac{1}{R_d^2}\right]\right\}, \tag{A6a}$$

while that of lateral dissipation on the right-hand side is

$$O\left\{\max\left[A_H\left(\frac{\beta}{2\sigma}\right)^4, A_H\left(\frac{3\pi}{L_x}\right)^4\right]\right\}. \tag{A6b}$$

Therefore, the dissipation time scales of eastward Rossby waves is found by solving Eqs. (A6a) and (A6b).

REFERENCES

Annamalai, H., and J. Slingo, 2001: Active/break cycles: Diagnosis of the intraseasonal variability of the Asian summer monsoon. *Climate Dyn.*, **18**, 85–102, doi:10.1007/s003820100161.

Bayler, J., and Z. Liu, 2008: Basin-scale wind-forced dynamics of the seasonal southern South China Sea Gyre. *J. Geophys. Res.*, **113**, C07014, doi:10.1029/2007JC004519.

Bretherton, C., M. Widmann, V. Dymnidov, J. Wallace, and I. Blade, 1999: The effective number of spatial degrees of freedom of a time-varying field. *J. Climate*, **12**, 1990–2009, doi:10.1175/1520-0442(1999)012<1990:TENOSD>2.0.CO;2.

Cessi, P., and S. Louazel, 2001: Decadal oceanic response to stochastic wind forcing. *J. Phys. Oceanogr.*, **31**, 3020–3029, doi:10.1175/1520-0485(2001)031<3020:DORTSW>2.0.CO;2.

Chan, J., W. Ai, and J. Xu, 2002: Mechanisms responsible for the maintenance of the 1998 South China Sea summer monsoon. *J. Meteor. Soc. Japan*, **80**, 1103–1113, doi:10.2151/jmsj.80.1103.

Chatterjee, P., and B. Goswami, 2004: Structure, genesis and scale selection of the tropical quasi-biweekly mode. *Quart. J. Roy. Meteor. Soc.*, **130**, 1171–1194, doi:10.1256/qj.03.133.

Chen, G., Y. Hou, and X. Chu, 2011: Mesoscale eddies in the South China Sea: Mean properties, spatiotemporal variability, and impact on thermohaline structure. *J. Geophys. Res.*, **116**, C06018, doi:10.1029/2011JD016244.

Chen, T., and J. Chen, 1993: The 10–20-day mode of the 1979 Indian monsoon: Its relation with the time variation of monsoon rainfall. *Mon. Wea. Rev.*, **121**, 2465–2482, doi:10.1175/1520-0493(1993)121<2465:TDMOTI>2.0.CO;2.

——, and ——, 1995: An observational study of the South China Sea monsoon during the 1979 summer: Onset and

life cycle. *Mon. Wea. Rev.*, **123**, 2295–2318, doi:10.1175/1520-0493(1995)123<2295:AOSOTS>2.0.CO;2.

Chen, Z., and L. Wu, 2011: Dynamics of the seasonal variation of the North Equatorial Current bifurcation. *J. Geophys. Res.*, **116**, C02018, doi:10.1029/2011JD016244.

Dee, D., and Coauthors, 2011: The ERA-Interim reanalysis: Configuration and performance of the data assimilation system. *Quart. J. Roy. Meteor. Soc.*, **137**, 553–597, doi:10.1002/qj.828.

Dibarboure, G., O. Lauret, F. Mertz, and V. Rosmorduc, 2008: SSALTO/DUACS user handbook: MSLA and (M)ADT near-real time and delayed time products. CNES Rep. SALP-MU-P-EA-21065-CLS, 35 pp. [Available online at http://www.aviso.oceanobs.com/fileadmin/documents/data/tools/hdbk_duacs.pdf.]

Ducet, N., P. Le Traon, and G. Reverdin, 2000: Global high-resolution mapping of ocean circulation from TOPEX/Poseidon and ERS-1 and -2. *J. Geophys. Res.*, **105**, 19 477–19 498, doi:10.1029/2000JC900063.

Fang, G., W. Fang, Y. Fang, and K. Wang, 1998: A survey of studies on the South China Sea upper ocean circulation. *Acta Oceanogr. Taiwan.*, **37**, 1–16.

Frankignoul, C., 1979: Stochastic forcing models of climate variability. *Dyn. Atmos. Oceans*, **3**, 465–479, doi:10.1016/0377-0265(79)90025-3.

——, P. Müller, and E. Zorita, 1997: A simple model of the decadal response of the ocean to stochastic wind forcing. *J. Phys. Oceanogr.*, **27**, 1533–1546, doi:10.1175/1520-0485(1997)027<1533:ASMOTD>2.0.CO;2.

Hu, J., H. Kawamura, H. Hong, and Y. Qi, 2000: A review on the currents in the South China Sea: Seasonal circulation, South China Sea Warm Current and Kuroshio intrusion. *J. Oceanogr.*, **56**, 607–624, doi:10.1023/A:1011117531252.

Isoguchi, O., and H. Kawamura, 2006: MJO-related summer cooling and phytoplankton blooms in the South China Sea in recent years. *Geophys. Res. Lett.*, **33**, L16615, doi:10.1029/2006GL027046.

Jia, Y., and Q. Liu, 2004: Eddy shedding from the Kuroshio bend at Luzon Strait. *J. Oceanogr.*, **60**, 1063–1069, doi:10.1007/s10872-005-0014-6.

Lau, K., and S. Yang, 1997: Climatology and interannual variability of the Southeast Asian summer monsoon. *Adv. Atmos. Sci.*, **14**, 141–162, doi:10.1007/s00376-997-0016-y.

Li, Y., W. Han, J. Wilkin, W. Zhang, H. Arango, J. Zavala-Garay, J. Levin, and F. Castruccio, 2014: Interannual variability of the surface summertime eastward jet in the South China Sea. *J. Geophys. Res. Oceans*, **119**, 7205–7228, doi:10.1002/2014JC010206.

Lin, X., J. Yang, D. Wu, and P. Zhai, 2008: Explaining the global distribution of peak-spectrum variability of sea surface height. *Geophys. Res. Lett.*, **35**, L14602, doi:10.1029/2008GL034312.

Liu, Q., X. Jiang, S. Xie, and W. T. Liu, 2004: A gap in the Indo-Pacific warm pool over the South China Sea in boreal winter: Seasonal development and interannual variability. *J. Geophys. Res.*, **109**, C07012, doi:10.1029/2003JC002179.

——, A. Kaneko, and J. Su, 2008: Recent progress in studies of the South China Sea circulation. *J. Oceanogr.*, **64**, 753–762, doi:10.1007/s10872-008-0063-8.

——, M. Feng, and D. Wang, 2011: ENSO-induced interannual variability in the southeastern South China Sea. *J. Oceanogr.*, **67**, 127–133, doi:10.1007/s10872-011-0002-y.

Liu, Z., H. Yang, and Q. Liu, 2001: Regional dynamics of seasonal variability in the South China Sea. *J. Phys. Oceanogr.*, **31**, 272–284, doi:10.1175/1520-0485(2001)031<0272:RDOSVI>2.0.CO;2.

Mao, J., and J. Chan, 2005: Intraseasonal variability of the South China Sea summer monsoon. *J. Climate*, **18**, 2388–2402, doi:10.1175/JCLI3395.1.

Murakami, T., and T. Nakazawa, 1984: On the 40–50 day oscillations during the 1979 Northern Hemisphere summer. Part I: Phase propagation. *J. Meteor. Soc. Japan*, **62**, 440–468, doi:10.2151/jmsj1965.62.3_440.

——, and ——, 1985: Tropical 45-day oscillations during the 1979 Northern Hemisphere summer. *J. Atmos. Sci.*, **42**, 1107–1122, doi:10.1175/1520-0469(1985)042<1107:TDODTN>2.0.CO;2.

Nan, F., H. Xue, and F. Yu, 2015: Kuroshio intrusion into the South China Sea: A review. *Prog. Oceanogr.*, **137**, 314–333, doi:10.1016/j.pocean.2014.05.012.

Pedlosky, J., 1987: *Geophysical Fluid Dynamics*. 2nd ed. Springer-Verlag, 710 pp.

Roxy, M., Y. Tanimoto, B. Preethi, P. Terray, and R. Krishnan, 2013: Intraseasonal SST-precipitation relationship and its spatial variability over the tropical summer monsoon region. *Climate Dyn.*, **41**, 45–61, doi:10.1007/s00382-012-1547-1.

Volkov, D., G. Larnicol, and J. Dorandeu, 2007: Improving the quality of satellite altimetry data over continental shelves. *J. Geophys. Res.*, **112**, C06020, doi:10.1029/2006JC003765.

Wang, B., and X. Xie, 1997: A model for the boreal summer intraseasonal oscillation. *J. Atmos. Sci.*, **54**, 72–86, doi:10.1175/1520-0469(1997)054<0072:AMFTBS>2.0.CO;2.

——, F. Huang, Z. Wu, J. Yang, X. Fu, and K. Kikuchi, 2009: Multiscale climate variability of the South China Sea monsoon: A review. *Dyn. Atmos. Oceans*, **47**, 15–37, doi:10.1016/j.dynatmoce.2008.09.004.

Wang, D., W. Wang, P. Shi, P. Guo, and Z. Gan, 2003: Establishment and adjustment of monsoon-driven circulation in the South China Sea. *Sci. China Ser. D*, **46**, 173–191, doi:10.1360/03yd9016.

——, and Coauthors, 2013: Progress of regional oceanography study associated with western boundary current in the South China Sea. *Chin. Sci. Bull.*, **58**, 1205–1215, doi:10.1007/s11434-012-5663-4.

Wang, G., D. Chen, and J. Su, 2006: Generation and life cycle of the dipole in the South China Sea summer circulation. *J. Geophys. Res.*, **111**, C06002, doi:10.1029/2005JC003314.

——, C. Wang, and R. Huang, 2010: Interdecadal variability of the eastward current in the South China Sea associated with the summer Asian monsoon. *J. Climate*, **23**, 6115–6123, doi:10.1175/2010JCLI3607.1.

——, L. Zheng, R. Wu, and C. Chen, 2013: Impacts of the Madden–Julian oscillation on the summer South China Sea ocean circulation and temperature. *J. Climate*, **26**, 8084–8096, doi:10.1175/JCLI-D-12-00796.1.

Xie, Q., X. Wu, W. Yuan, D. Wang, and S. Xie, 2007: Life cycle of intraseasonal oscillation of summer SST in the western South China Sea. *Acta Oceanol. Sin.*, **3**, 1–8.

Xie, S., Q. Xie, D. Wang, and W. T. Liu, 2003: Summer upwelling in the South China Sea and its role in regional climate variations. *J. Geophys. Res.*, **108**, 3261, doi:10.1029/2003JC001867.

——, C. Chang, Q. Xie, and D. Wang, 2007: Intraseasonal variability in the summer South China Sea: Wind jet, cold filament, and recirculations. *J. Geophys. Res.*, **112**, C10008, doi:10.1029/2007JC004238.

Yang, H., L. Wu, H. Liu, and Y. Yu, 2013: Eddy energy sources and sinks in the South China Sea. *J. Geophys. Res. Oceans*, **118**, 4716–4726, doi:10.1002/jgrc.20343.

Zeng, L., and D. Wang, 2009: Intraseasonal variability of latent-heat flux in the South China Sea. *Theor. Appl. Climatol.*, **97**, 53–64, doi:10.1007/s00704-009-0131-z.

Zhuang, W., S. Xie, D. Wang, B. Taguchi, H. Aiki, and H. Sasaki, 2010: Intraseasonal variability in sea surface height over the South China Sea. *J. Geophys. Res.*, **115**, C04010, doi:10.1029/2009JD013165.